*ISSN 1392-1207. MECHANIKA. Vol. 31, No. 6, 2025: 541–553*

# Fail-Safe Mass Reduction of a Heavy-Duty Front Axle Using Topology Optimisation

**Kübra POLAT*, Mehmet Murat TOPAÇ**, Ufuk ÇOBAN*****
**The Graduate School of Natural and Applied Sciences, Dokuz Eylül University, Izmir 35397, Türkiye,*
*E-mail: k.polat@ogr.deu.edu.tr*
***Department of Mechanical Engineering, Dokuz Eylül University, Izmir 35397, Türkiye,*
*E-mail: murat.topac@deu.edu.tr*
****BMC Automotive Industry and Trade Inc, Heavy Commercial Vehicles Division, Izmir 35060, Türkiye,*
*E-mail: ufuk.coban@bmc.com.tr*
https://doi.org/10.5755/j02.mech.42930

## 1. Introduction

Axles are critical components that have a significant impact on vehicle performance and safety. Axles maintain the distance between the wheels and the horizontal position of the wheels relative to the vehicle body. In heavy – duty vehicles, front and rear axles have different designs due to their different functions [1, 2]. While the non – driven rigid front axle usually performs steering and load carrying tasks, the rear axle is often integrated into the drivetrain and plays a role in power transmission. In commercial vehicles, the rigid front axle is often not considered as part of the drivetrain [3].

A front axle housing usually consists of an *I-section* beam extending from one spring seat to the other. The axle housing can exhibit different design variations depending on the layout of the vehicle structural elements [3, 4]. A downward curved design provides more space for the engine, allowing assembly to be carried out at lower levels, while an upward curved front axle housing offers a high degree of ground clearance [4, 5]. Fig. 1 shows a typical front axle structure used in heavy commercial vehicles.

The load conditions to which the front axle is subjected vary depending on different driving conditions. Therefore, the axle structure needs to be optimised to resist various driving behaviours [4]. Especially when braking is applied during cornering, the acceleration of the vehicle body causes an increase in the front axle load and a simultaneous decrease in the load on the rear axle. There is also a load transfer between the wheels of the axle depending on the direction of rotation. During braking, the front axle is subjected to approximately 70% of the total load, assuming the load transfer due to braking at the wheels and bending loads due to the load carried by the vehicle [6, 7]. The load conditions representing the various driving conditions can be found in the open literature [8]. All these load conditions are critical in axle design and must be taken into account during the design process [9, 10].

When designing the front axle geometry, factors such as straight-line stability, steering response and tyre wear must be optimised to suit the overall behaviour of the vehicle [4]. On the other hand, the axle beam accounts for about 10% of the unsprung mass [11, 12]. Reducing the unsprung mass is of great importance to improve the ride comfort and handling of the vehicle. For this reason, the design of the axle housing has long been considered in the context of lightweighting studies [1, 13, 14].

a

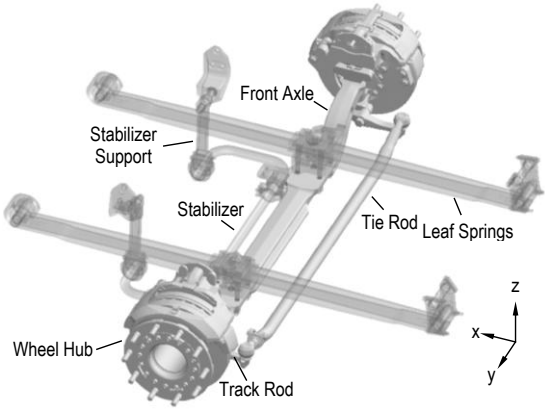


b

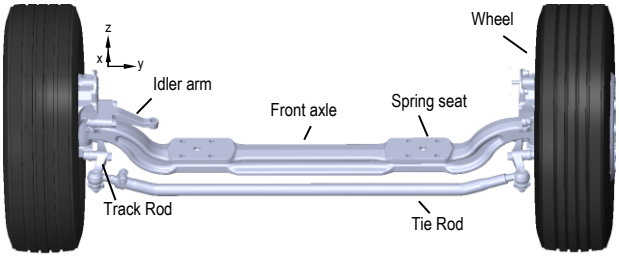


c

Fig. 1 Design example [Courtesy of BMC Automotive Industry and Trade Inc.]: a – heavy-duty commercial truck, b – front axle assembly, c – structure of the front axle beam

In this study, the optimum lightweight structure of a heavy commercial vehicle front axle was examined by an approach combining Finite Element Analysis (FEA), Topology Optimisation and Design of Experiments (DoE) methods. FEA was performed to determine the critical loading condition among those given in the literature. Topology optimisation was then performed to design a lightweight structure. DoE was applied to determine the optimum locations and dimensions of the mass reduction regions obtained from the topology optimisation. As a result of these analyses, a lighter front axle geometry was obtained. The improvements provided by the new design in terms of efficient use of axle material are examined.

To the best of the authors' knowledge, there is no study in the literature on the lightweighting of a heavy commercial vehicle front axle using topology optimisation and the effect of this lightweighting on the efficient use of its material.

This study aims to fill the existing gap in the literature and also presents a method to reduce part material costs and summarises this method through an industrial case study.

## 2. Load Model

In the early stages of chassis and suspension design, load cases based on standard driving maneuvers are used instead of actual load cases, as wheel loads are often not available or are measured with prototypes [8]. In the most common driving conditions, drive, brake and side forces act on a vehicle wheel in addition to the vertical load [15]. The load cases given in the literature can be considered as a combination of the mentioned forces. In other words, the wheel acceleration components of these load cases in Cartesian coordinates are a coefficient for the forces expected to act on the wheel contact point in the static state [8].

In the load cases used in this study, it is assumed that the vertical load acting on the front axle of the vehicle in the static state is applied equally to the wheels. The forces acting on the wheel contact point for bumping, turning and turning braking conditions are given schematically and graphically in Fig. 2. Each load type has an acceleration component in three axes. For these load conditions, the load of the stationary vehicle in the vertical direction ($z$ direction) is considered as a reference unit and the other loads are proportional to this load condition.

In the field test shown in Fig. 3, a road with a total length of 12,990 meters was preferred as the test path. When the instantaneous acceleration data obtained from the vehicle during the test phase given in Fig. 3, b is analyzed, it is determined that the maximum acceleration value is 2.6$G$. This value is consistent with the results in the literature.

## 3. Material and Methods

### 3.1. Material

The material choice in front axle manufacturing must be light and provide high rigidity to the axle. The

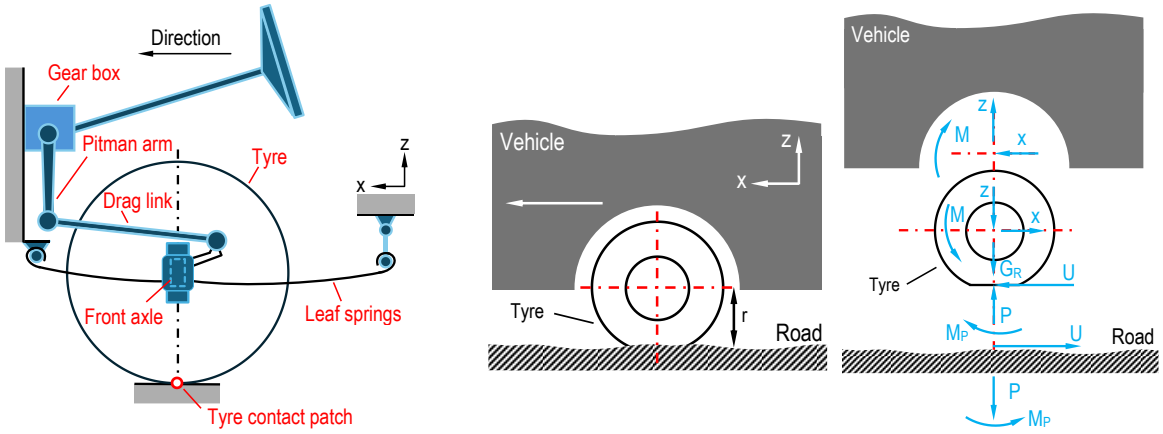


a b

| | Load Cases | x | y | z |
|---|---|---|---|---|
| 1 | Stationary Vehicle | 0 | 0 | 1 |
| 2 | Vertical Bump (3.0 G) | 0 | 0 | 3 |
| 3 | Longitudinal Bump (2.50 G) | 2.5 | 0 | 1 |
| 4 | Lateral Bump (2.50 G) | 0 | 2.5 | 1 |
| 5 | Cornering Right (1.25 G) | 0 | 1.25 | 1 |
| 6 | Braking & Cornering | 0.75 | 0.75 | 1 |
| 7 | Braking in reverse (1.0 G) | 1 | 0 | 1 |
| 8 | Acceleration (-0.5 G) | -0.5 | 0 | 1 |
| 9 | Accelerating & Cornering (0.7 G) | -0.5 | 0.5 | 1 |
| 10 | Diagonal Load (front & rear) | 0 | 0 | 1.75 |
| 11 | Vertical Bump (2.25 G) | 0 | 0 | 2.25 |
| 12 | Vertical Rebound (0.75 G) | 0 | 0 | 0.75 |
| 13 | Cornering Right (0.75 G) | 0 | 0.75 | 1 |
| 14 | Cornering Left (0.75 G) | 0 | -0.75 | 1 |
| 15 | Braking (0.75 G) | 0.75 | 0 | 1 |
| 16 | Acceleration (0.5 G) | -0.5 | 0 | 1 |

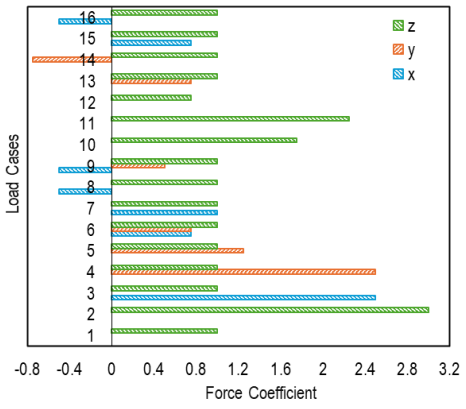


c

Fig. 2 Load cases: a – schematic view of the front axle [5], b – forces acting at the wheel contact point [16], c – force coefficients for various driving conditions [8]

Table 1

The chemical composition and mechanical properties of 42CrMo4

| The Chemical Composition | | | | | | | | | | |
|---|---|---|---|---|---|---|---|---|---|---|
| C | Si | Mn | P | S | Cr | Mo | Ni | Al | Cu | Sn |
| 0.4 | 0.3 | 0.83 | 0.009 | 0.026 | 1.14 | 0.24 | 0.15 | 0.027 | 0.15 | 0.008 |
| The Mechanical Properties | | | | | | | | | | |
| $S_{ut}$ (MPa) | | | $S_y$ (MPa) | | | *HB* | | | *A* | |
| 1300 | | | 877 N/mm$^2$ | | | 269-320 | | | %10 | |

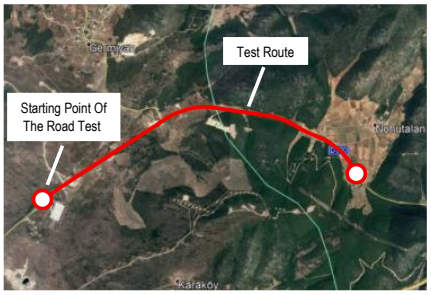


a

b

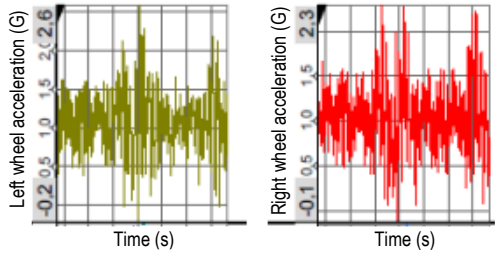


c

Fig. 3 Test facility: a – test route, b – test vehicle, c – vertical wheel accelerations

manufacturer uses 42CrMo4 in front axle manufacturing. The chemical composition and mechanical properties of this material obtained from the manufacturer are given in Table 1. Here, $S_{ut}$, $S_y$, *HB* and *A* represents tensile strength, yield strength, hardness and elongation respectively.

### 3.2. Topology optimization

Topology optimization is one of the most common type of structural optimization methods. It is used to estimate the optimum material distribution within a given initial design space of the structure at the initial design phase. The topology, shape and size of the structure are not represented by standard parametric functions, but by many functions defined over a constant design space. These functions are used to find the optimal material distribution for the target feature [17]. Shortly, it aims to find the optimal load path for a given load and boundary condition [18]. One of the most popular mathematical methods for topology optimization is the Solid Isotropic Material with Penalization (SIMP) method. The SIMP method estimates the optimum material distribution within a given design space for various load cases, boundary conditions, manufacturing constraints and performance requirements. In this method, a penalty factor is used so that the intermediate densities assume values closer to zero or one, thus avoiding the formation of grey regions of intermediate densities [19]. The density distribution of material, $\rho$, within a design space is discrete and each element is assigned a value in two variables where $\rho$ is either 1 (where material is required) or 0 (where material is removed). In the SIMP approach, the relationship between the density design variable and the material property;

$$E_{ijkl}(x) = \rho(x)^p \, E_{ijkl}{}^0, \, p > 1, \tag{1}$$

$$\int_\Omega \rho(x) d\Omega \le V, \; 0 \le \rho(x) \le 1, \; x \in \Omega \, . \tag{2}$$

Here $p$ is the penalization parameter, $\rho$ is the density and $E$ is Young's modulus.

For $p = 1$, the optimization problem corresponds to the "variable – thickness – sheet" problem, which is a convex problem [17, 20]. In this case, the material stiffness changes linearly with density and the optimization process becomes simple. A value of $p > 1$ decreases the stiffness/volume ratio, thus making intermediate density unsuitable [18]; $p$ values of 3 or greater are assumed to have good results for both 2D and 3D structures [18, 19]. It is important to note that the penalization effect is only effective in the presence of a volume constraint or some other constraint that indirectly limits the volume. In the absence of these constraints, penalization does not give the expected result and the optimization process is not effective. SIMP usually starts with a homogeneous distribution of densities in the design space and a specified volume fraction. The first step of the iterative analysis is the solution of the equilibrium equations, followed by a sensitivity analysis that calculates the derivatives of the design variables (e.g. element densities). To provide the numerical stability, filtering techniques are applied before the densities are updated using minimum suitability criteria, followed by a new FEA. This procedure is repeated until convergence is achieved.

### 3.3. DoE-RSM

DoE (Design of Experiments) and Response Surface Methodology (RSM) were used via the DesignXplorer™ module of ANSYS/Workbench™ to obtain the final geometry with the parameters selected from the geometry obtained from topology optimization. DoE – RSM is a numerical method used in parametric optimization applications. It determines the relationships between the geometrical parameters of a structure and the system response to

variables such as maximum stress or deformation under defined loading conditions. Depending on the number of input parameters, design points are defined by the software, and for the responses at these points, the input parameters have various variable values. Then, FEA is repeated at these points and the desired system response is determined. RSM, on the other hand, is used to generate a continuous function of the output parameters in terms of the geometric input parameters and this function is visualized as a surface to represent the system response. RSM uses a polynomial regression model, which can be expressed as follows [21]:

$$\boldsymbol{y} = \boldsymbol{\beta}_0 + \sum_{i=1}^{k} \boldsymbol{\beta}_i \boldsymbol{x}_i + \sum_{i \le j}^{k} \boldsymbol{\beta}_{ij} \boldsymbol{x}_i \boldsymbol{x}_j + \boldsymbol{\varepsilon}\,; \tag{3}$$

matrix form is as follows:

$$\boldsymbol{y} = \boldsymbol{X\beta} + \boldsymbol{\varepsilon}\,. \tag{4}$$

Here, $\boldsymbol{y}$ is the observation vector, $x$ is the model matrix, $\boldsymbol{\beta}$ is the vector of partial regression constants and $\boldsymbol{\varepsilon}$ is the error vector.

### 3.4. Workflow

The front axle investigated in this study has a suitable structure that is used in the heavy commercial vehicle segment and meets the safety requirements. Firstly, the test conditions specified in the literature were simulated with FEA on this axle virtual model. According to the results of this analysis, the critical loading condition causing higher stress concentration was determined and this case was used to determine the regions suitable for mass reduction on the front axle within the scope of topology optimization. After the topology optimization, a DoE – based mitigation study was carried out in the lower region of the spring table based on the seven parameters determined. The fatigue life analysis of the new geometry was carried out by considering the notch effect of the discharges created for lightening. The flowchart of the method applied within the scope of the study is given in Fig. 4.

## 4. Results and Discussion

### 4.1. Finite element model and results

The front axle solid model was imported into ANSYS® Workbench 2020R2 commercial FEA software to determine the critical load condition. The analysis model consists of a total of five elements: two supports, one front axle model and two axles as shown in Fig. 5, c. In order to simulate the road conditions, the reference model is placed on the supports, labelled as points *C* and *D* in Fig. 5, a. The distance between the contact points of the supports is equal to the vehicle track width (*t*). Vertical loads were applied at points *A* and *B*, which are defined as spring mounting surfaces. The distance *H* between the wheel contact point and the wheel rotation axis is determined by the dimensions of the tires used on the vehicle, as shown in Fig. 5, b.

In the Finite Element (FE) model of the axle, SOLID187 elements were used, each consisting of a total of ten nodes with three linear degrees of freedom. The FE model contains a total of 202,445 elements and 324,198 nodes.

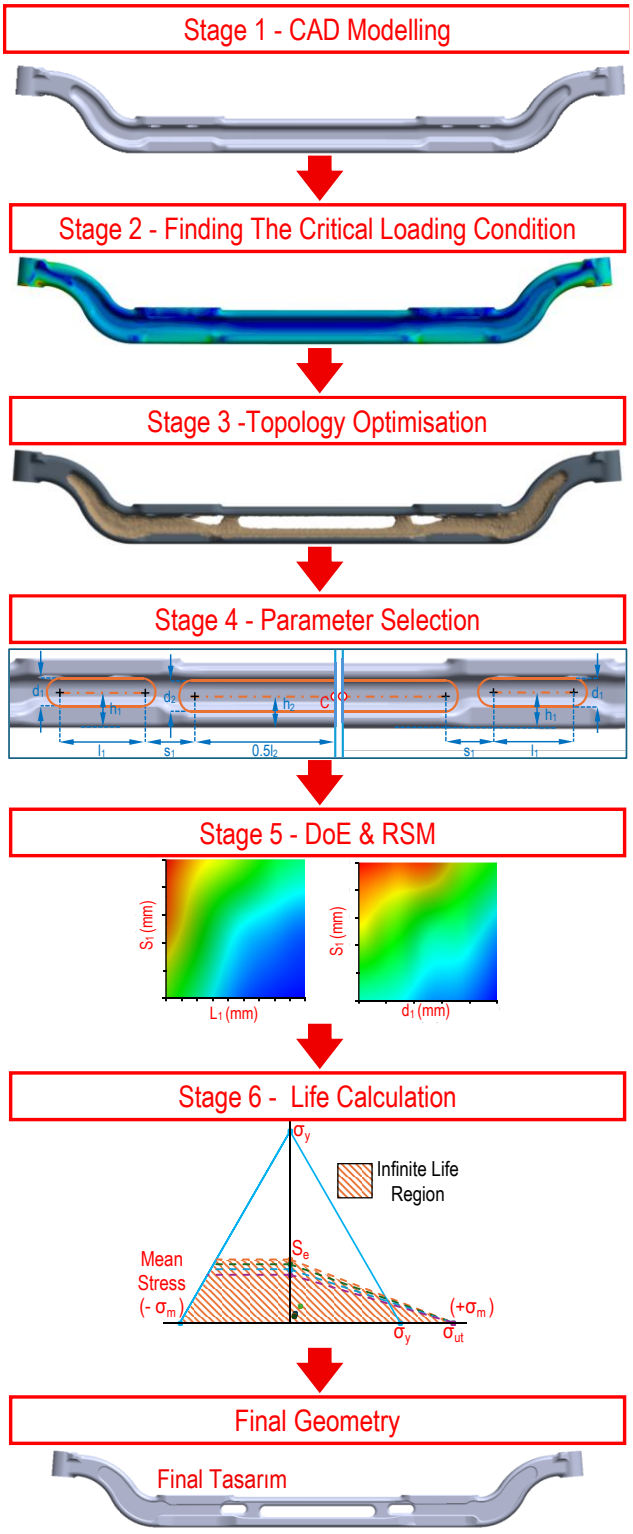


Fig. 4 Flowchart of the study

### 4.2. Determination of critical load case

In the first stage of the study, the front axle body was considered as a simple beam model as shown in Fig. 6, a and the stress distribution was analyzed through a selected section on the axle body. According to the results of the analysis, it was found that the lowest stress concentration occurred in the neutral axis region and the highest stress concentration occurred in the region farthest from the neutral axis. These high stress regions are labelled as $CP_1$ and $CP_2$ in Fig. 6, b. The stress behavior of these regions was

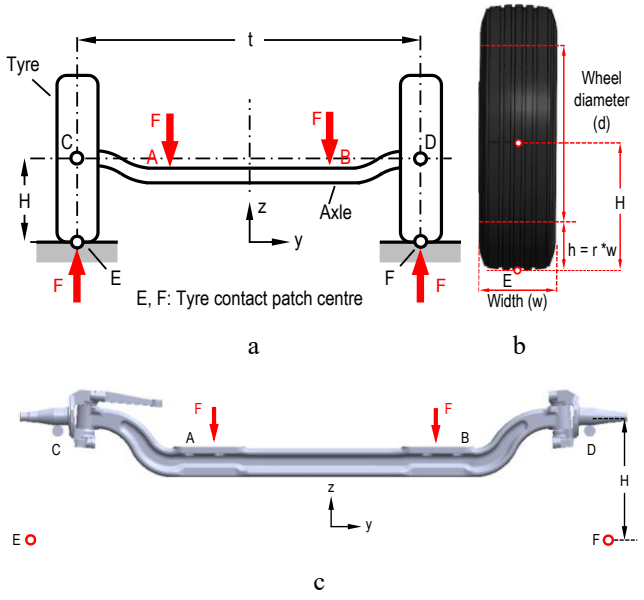


Fig. 5 Load model: a – free body diagram of the front axle, b – wheel dimensions, c – loads and boundary conditions used in the FE analysis

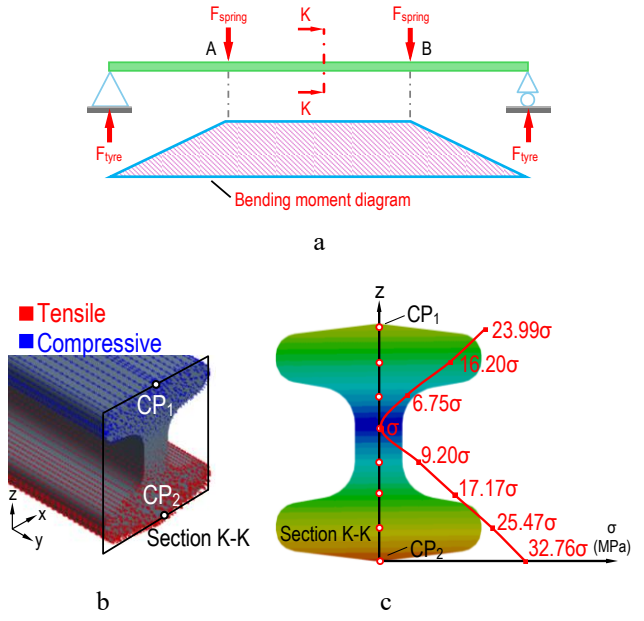


Fig. 6 Idealisation of the loading case: a – bending moment diagram, b – principal stress distribution, c – von Mises stress distribution on the cross-sectional area

also investigated. The $CP_2$ area subjected to tensile stress was considered to be a potential damage zone and this area was defined as the critical zone. The stress change graph and stress behavior of the section are given in Fig. 6, b.

In order to compare the effects of the load cases given in Fig. 2, c on the von Mises stress concentration, thirteen points ($P_1 – P_{13}$) were determined from the region ($CP_2$) where the towing effect on the axle is the highest. The equivalent von Mises stress values at these points under different loading scenarios are compared in Fig. 7.

According to the results of the analyses, the point $P_{13}$ at Cornering Right ($0.75G$), which has the lowest stress value, was accepted as a reference and the stress value of this point was scaled as one unit. The stress values obtained in other loading scenarios ($\sigma_{Pn}$) were proportioned based on point $P_{13}$ and shown on the graph. According to the graph,

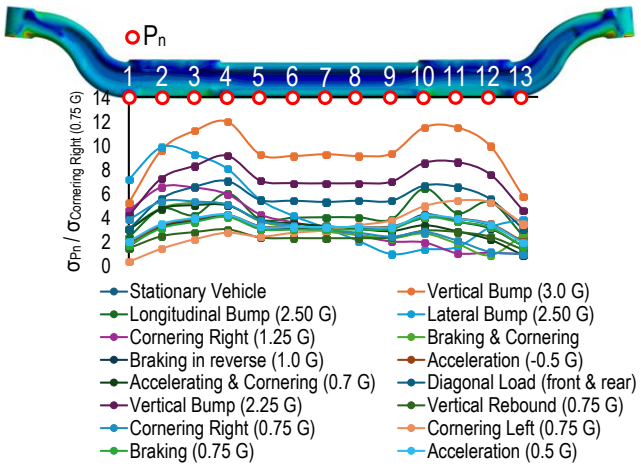


Fig. 7 Comparison of von Mises stress distributions for various load cases

the highest stress concentration occurred at all points in the Vertical Bump ($3G$) loading case. This critical loading case was used in topology optimization to determine the regions of the front axle suitable for mass reduction, and then DoE –based parametric optimization was applied to determine the optimal location and dimensions of these regions.

### 4.3. Mass reduction of front axle by topology optimisation

The topology optimization was performed using ANSYS® Workbench software. Initially, design regions where mass reduction is achieved and exclusion regions where the material will not be removed were determined. In Fig. 8, a, the defined exclusion zones are shown in red and design zones are shown in blue. The topology optimization was performed by defining a response constraint that aims to reduce the mass of the new geometry while maintaining 25% of the mass of the reference model. The final model obtained is shown in Fig. 8, b.

Preliminary studies for parametric optimization were carried out using the geometries extracted from the regions suitable for mass reduction obtained as a result of the analysis. The geometries extracted for this mass reduction not only reduce the mass of the axle beam, but can also affect the deformation of the axle. This deformation may affect the camber angle of the wheels depending on the stiff-

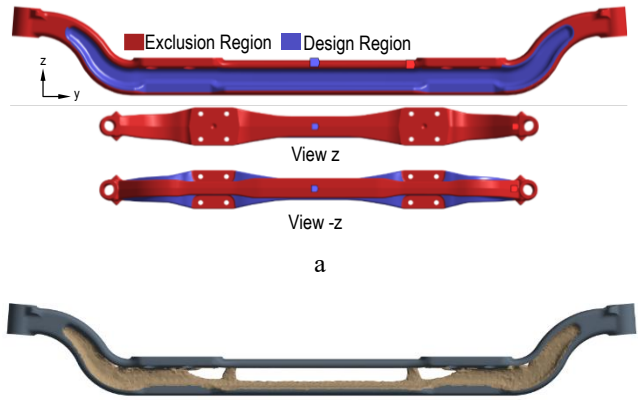


Fig. 8 Topology optimization of the axle beam: a – regions defined in the software for topology optimisation, b – the result of topology optimization

ness of the axle.

Therefore, the dynamic behavior of the vehicle should be taken into account in addition to stress analyses when locating the mass reduction zones or determining the hole shape. Such modifications can lead to potential changes that can affect the handling or maneuverability of the vehicle, so it is important to balance both factors.

To achieve this balance, both the stress distribution and the dynamic response of the vehicle need to be optimized.

### 4.4. Determination of output parameters for DoE-based optimisation

The point *M* given in Fig. 9 was repositioned for six selected points ($P_1 - P_6$) and the effect of these position changes on the wheel camber angle was analyzed. In the graph, the angle ($\alpha^\circ$) obtained for the reference geometry is considered as one unit and the other points are proportioned according to this reference value. According to the results of the analysis, it was determined that the slot placed at any point on the axle body increases the camber angle with a maximum value as low as approximately 0.10.

According to the simple beam approach given in Fig. 6, the center region of the axle is located on the neutral axis and is therefore considered as the minimum stress region. The geometrical shapes of the slots created for mitigation in this region were evaluated. According to the results of the topology analysis, two different models were created and the effect of the mitigation work to be performed in this region was evaluated. Fig. 10 shows the variation graphs of the geometries named as Reference, Model *A* and Model *B* with respect to each other in terms of mass, camber angle and equivalent stress. In all graphs, the values in the reference model are considered as one unit and the values of

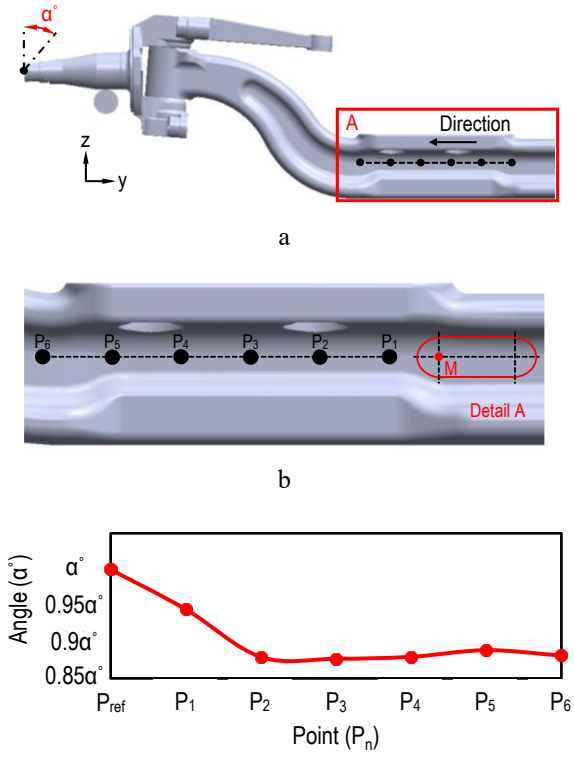


Fig. 9 Effect of mass reduction on wheel camber: a – camber angle, b – mitigation zone, c – camber alteration

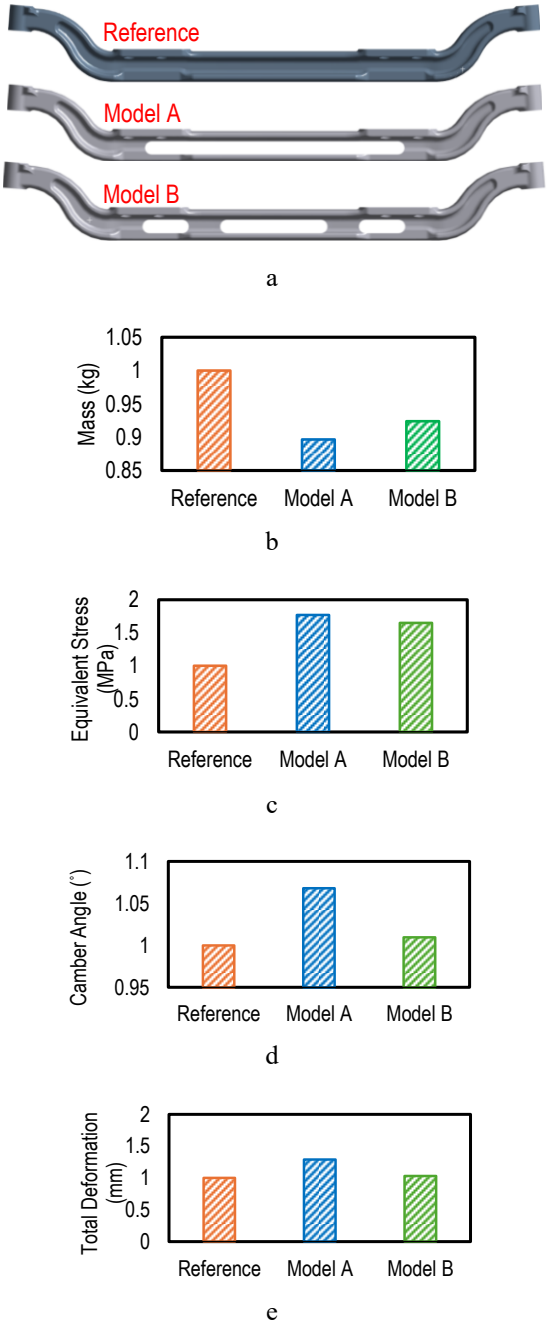


Fig. 10 Design models and variation graphs: a – the preliminary beam structures for DoE, b – mass variation, c – equivalent stress variation, d – camber angle variation, e – total deformation variation

Model *A* and Model *B* are proportioned according to this reference.

Although the mass of Model *A* was reduced by about 10% compared to the reference model, only a very small change of 0.05 degrees in the camber angle was observed. The results of Fig. 9 and Fig. 10 show that the weight reduction has no significant effect on the camber angle. Therefore, the camber angle was not selected as an output parameter in the DoE step. In addition, a stress increase of about 77% was observed in Model *A* under the spring seat region. Model *B* showed a lower stress increase and total deformation in this region. The reason for this is that the slots in Model *B* form a lattice structure that allows the loads to be distributed more evenly throughout the body. Changing the size and position of these slots will directly affect the

stress and total deformation by causing differences in the lattice structure. Therefore, Model *B* was considered to be suitable for DoE– based optimization and the dimensions and locations of these slots were selected as input parameters.

4.5. DoE-based optimization

Using the preliminary study and topology optimisation analyses, a preliminary idealised model of the slots is shown in Fig. 11. The idealised CAD design of these slots was built using implemented [4] slot examples and implemented in the DoE study.

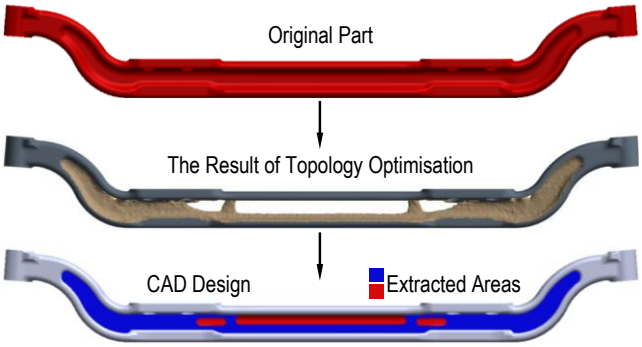


Fig. 11 The axle beam obtained after topology optimisation and the idealised geometry for DoE

In the model created for DoE – based optimization, seven parameters including the size and position of the slots were determined. The parameters given in Fig. 12 are shown as slot diameters (*d*), widths (*l*), the height of the slot center point to the base (*h*) and the distance between the slots (*s*). The slot shapes in the areas shown as *A* and *B* are defined to be symmetrical to each other with respect to the axis symmetry point *C*. With these selected parameters, the mass, total deformation and in-slot equivalent stress of the front axle for the design points generated by the software were selected as output and the design table was created. The parameter variation range was chosen in such a way that the axle integrity is not disturbed.

Some of the samples generated by the software are

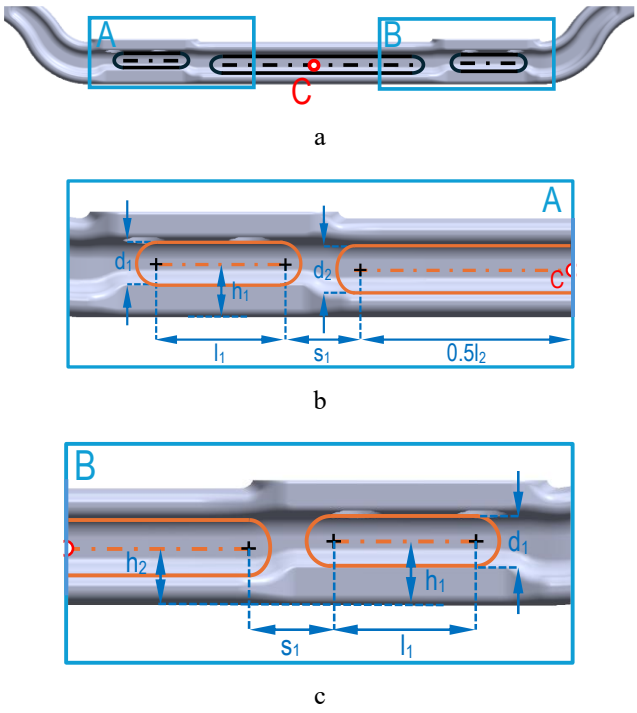


Fig. 12 The parameters for DoE-based optimization: a – mitigation zones, b – detail A, c – detail B

given in Fig. 13. The regions shown in red represent the volumes where mass reduction was performed. Also, the numerical values of the parameters are in millimetres (mm). While obtaining the optimum parameter values from the RS graphs, the condition that the stress value of the housing and the axle mass should be minimum was defined as the design target. In addition, it is aimed not to create a new fracture zone or mode in the part body as a result of lightweighting. Fig. 14 shows the maximum von Mises stress variation graphs obtained from the slot regions of the part as a result of the parametric study. In the graphs, the minimum stress value is considered as a unit and other values are presented as a ratio to this reference value.

Fig. 15 shows the percentages of influence of the design parameters on the mass and equivalent stress. When the graph is analyzed, it is seen that the diameter parameter

| | | | |
|---|---|---|---|
| Extracted Areas | $R_2 = 20$<br>$H_2 = 20.5$<br>$L_2 = 255$ | $R_1 = 10$<br>$H_1 = 15.5$<br>$L_1 = 110$ | $S_1 = 125$ |
| | $R_2 = 20$<br>$H_2 = 0$<br>$L_2 = 255$ | $R_1 = 20$<br>$H_1 = 15.5$<br>$L_1 = 110$ | $S_1 = 125$ |
| | $R_2 = 20$<br>$H_2 = 20.5$<br>$L_2 = 255$ | $R_1 = 20$<br>$H_1 = 15.5$<br>$L_1 = 110$ | $S_1 = 50$ |
| | $R_2 = 20$<br>$H_2 = 20.5$<br>$L_2 = 255$ | $R_1 = 14.7$<br>$H_1 = 7.83$<br>$L_1 = 157.6$ | $S_1 = 85.3$ |
| | $R_2 = 14.7$<br>$H_2 = 10$<br>$L_2 = 384.6$ | $R_1 = 25.3$<br>$H_1 = 7.83$<br>$L_1 = 157.6$ | $S_1 = 85.3$ |

Fig. 13 Some selected examples from the design table

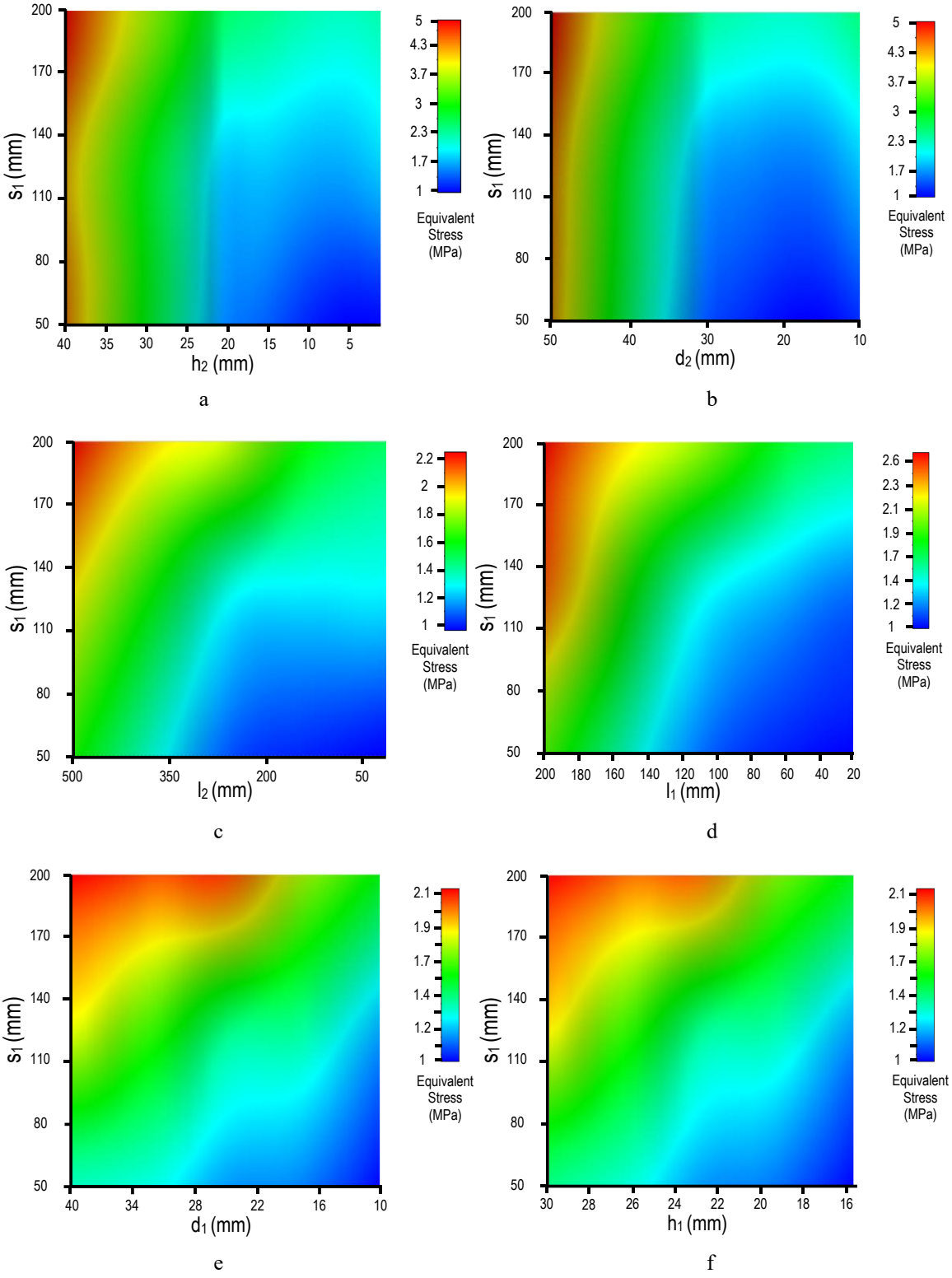


Fig. 14 Response surface plots for equivalent stress values. The vertical axis ($y$) represents the value of parameter $s_1$ and the horizontal axis ($x$) represents respectively: a – $h_2$, b – $d_2$, c – $l_2$, d – $l_1$, e – $d_1$ and f – $h_1$

$d_2$ has the highest negative effect on the mass, but shows the largest positive effect on the equivalent stress. This indicates that increasing $d_2$ can increase the equivalent stress while significantly decreasing the mass. The parameter $h_2$ shows a similar trend, causing a decrease in mass while increasing the equivalent stress. In contrast, the parameters $l_1$, $d_1$ and $h_1$ have relatively low effects on both mass and equivalent stress.

The parameter $s_1$ has a small positive effect on the equivalent stress, while its effect on the mass is quite limited. Changes to be made in certain parameters with high effect percentages for both output parameters are important in terms of balancing between mass reduction and stress increase. When the stress distributions of different points on the front axle are analyzed, it is seen that there is stress concentration in the lower region of the spring seat of the axle body as shown in Fig. 16.

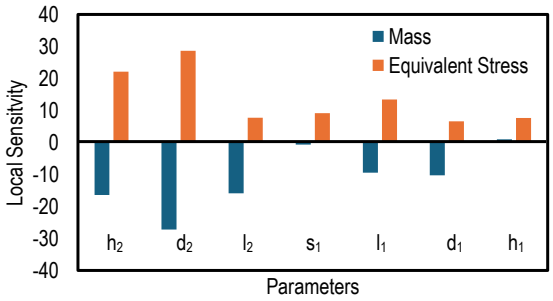


Fig. 15 Local sensitivity (%) of the effect on mass and stress

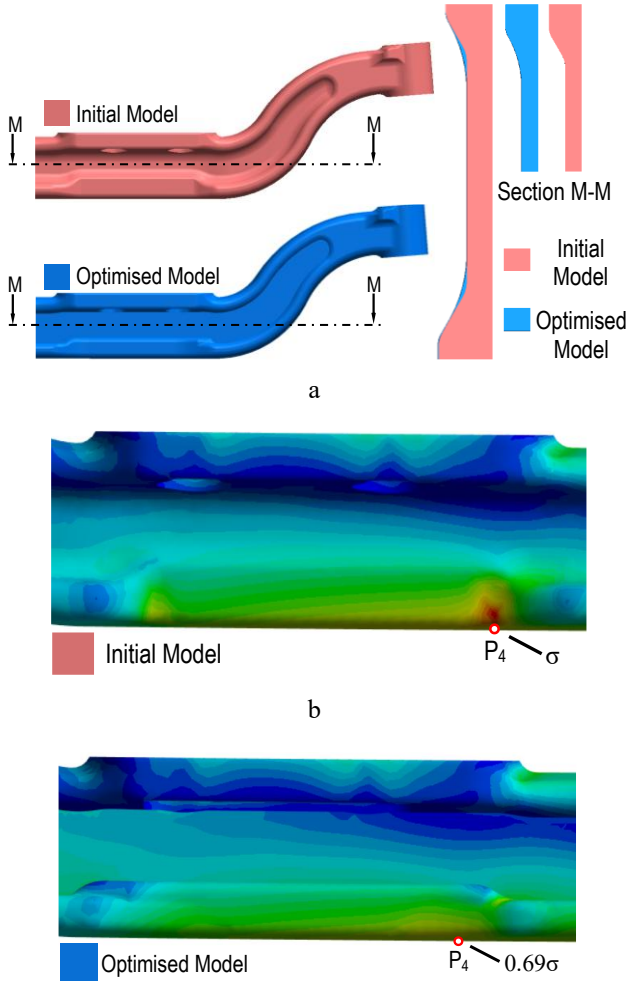


a

b

c

Fig. 16 Design modification: a – initial and optimized model structures, FEA results of: b – initial model, c – optimized model

Although the current design provides the desired life, service life and stress values, these regions should be evaluated separately due to the stress increase and notch effect caused by the hole to be opened on the body for mass reduction.

For this purpose, considering the sudden cross-sectional change occurring in the transition zone and the fact that the zone is subjected to tension stress, the cross-sectional transition in this zone was softened in order to prevent the stress levels from reaching the damage limit after mass reduction. Fig. 16, a shows the new axle model resulting from the DoE – based optimization and FEA. A total mass reduction of 14.2% was achieved with the new front axle design. The axle body may be subjected to dynamic cyclic stresses and fatigue damage during its service life. In the literature, there are studies based on experiments and simulations on fatigue failure analysis of an axle beam with a slot [22]. These studies provide findings for identifying critical regions and optimizing design modifications to improve fatigue resistance in similar designs. For this purpose, life calculation was carried out in this study to evaluate the effect of lightweighting of the axle geometry on the failure condition.

The propagation of a crack, the length of which is considered as a macro crack, in the plane perpendicular to the maximum tensile stress is one of the fatigue damage stages [23]. For this reason, in the final geometry, the regions of the mass reduction slots operating under tensile stress were identified and determined as critical areas in terms of fatigue strength. These areas are given in Fig. 17, b.

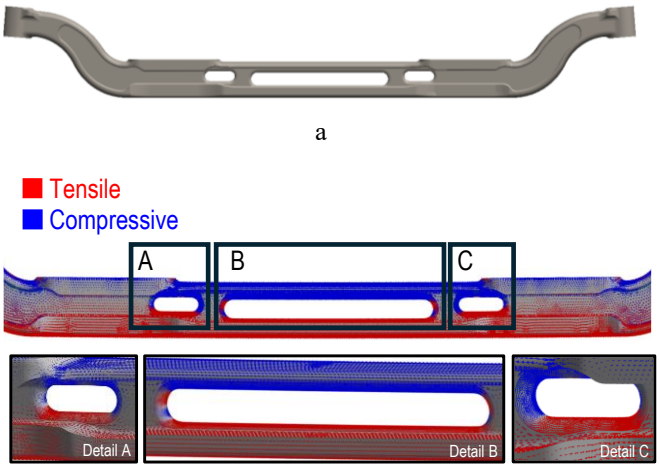


a

b

Fig. 17 Final design: a – model structure, b – principal stresses on the axle body

4.6. Life maps

While reducing the mass of the axle beam by topology optimization, structural safety should not be compromised. Fatigue strength is a critical design criterion for components subjected to variable loading conditions such as axle beams. In this context, the Goodman – Haigh diagram used in the literature [24-26] was preferred to evaluate the fatigue life of the component. The Goodman – Haigh diagram helps to determine the fatigue limits of the material by graphically presenting the relationship between the average stress and the alternating stress. The Goodman – Haigh diagram is used to check whether the cyclic stress history for a product made of a given material is within the infinite life region [27, 28]. If the design points lie below the modified Goodman line, the design is considered as safe. In this study, after determining the mass reduction zones in the axle beam, the maximum stress values obtained were evaluated on the Goodman – Haigh diagram and checked whether they remained within the safe operating range.

For steels with tensile strength $S_{ut}$ lower than 1400 MPa, the stress – life limit ($S_e'$) is given in the literature as [29]:

$$S_e' = 0.504 \times S_{ut} . \quad (5)$$

However, it is not realistic to expect the durability

limit of a mechanical or structural element to match exactly with the values obtained in the laboratory environment. This depends on various parameters such as material composition, effect of manufacturing method, heat treatment, surface condition, friction and corrosion. Considering the effect of factors such as surface condition, size, loading mode and temperature, Marin expresses the stress – life endurance limit ($S_e$) as follows [29]

$$S_e = k_a \cdot k_b \cdot k_c \cdot k_d \cdot k_e \cdot S_e^{'}. \tag{6}$$

Here, $k_a$ is a surface factor, $k_b$ is a size factor, $k_c$ is a load factor, $k_d$ is a temperature factor and $k_e$ is a fatigue – strength – reduction factor. In the calculation of $k_a$, the surface factor coefficients $a$ and $b$ for hot forging were taken as 57.7 and -0.718, respectively [29]. Using these coefficients, the surface factor ($k_a$) for SAE 4140 (42CrMo) material with a tensile strength ($S_{ut}$) of 1300 MPa was calculated as 0.335 [9, 30, 31]. The $k_b$ can be expressed for the bending and torsion cases as follows:

$$k_b = \begin{cases} (1.24d)^{-0.107} & 2.79 \le d \le 51\,\text{mm} \\ (1.51d)^{-0.157} & 51 < d \le 254\,\text{mm} \end{cases}. \tag{7}$$

The 95% stress field for the wide flanged section can be calculated by considering the values given in Fig. 18 [29]. Diameter $d$ value was determined by calculating 95% stress area for all axes. Using this value, the $k_b$ coefficient was found as 0.75 according to Eqs. (7) and (8). $k_c$ is given as 1 for bending and $k_d$ is taken as 1 for ambient temperature range (0 – 250 °C) [29].

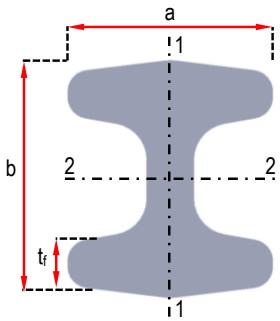


Fig. 18 The wide flanged section

$$A_{0.95\sigma} = \begin{cases} 0.10at_f & axis\,1-1 \\ 0.05ba \quad t_f > 0.025a & axis\,2-2 \end{cases}. \tag{8}$$
$$A_{0.95\sigma} = 0.0766d^2$$

To determine the maximum stress due to irregularities or defects, a stress concentration factor ($K_t$ or $K_{ts}$) has been defined, which is used as a multiplier of the nominal stress. The $K_f$ factor is often referred to as the fatigue stress concentration factor. Due to the increased sensitivity to notches, $K_f$ is considered as a stress concentration factor reduced from $K_t$ and is defined by Eq. (9). Notch sensitivity ($q$) is defined by Eq. (10), usually taking values ranging from zero to one. If $q$ is equal to zero, the material is insensitive to notches and the $K_f$ value is one. In addition, if $q$ is equal to one, the material is fully notch sensitive and $K_f$ and $K_t$ are equal to each other [29].

$$K_f = \frac{Maximum\ stress\ in\ notched\ specimen}{Stress\ in\ notch-free\ specimen}, \tag{9}$$

$$q = \frac{K_f - 1}{K_t - 1}. \tag{10}$$

In this study, FEA was used to calculate the $K_t$ value. Due to the vertical acceleration of the vehicle body due to road surface unevenness, the maximum dynamic load on the axle body was estimated as 2.25 times $P$ [8]. Firstly, the geometrical structures in regions $A$, $B$ and $C$ shown in Fig. 19, a were analysed and the higher stress concentration regions operating under tensile stress were determined for the initial and final design models. According to the results of the analyses, it was found that the highest stress value occurs equally and symmetrically in regions $A$ and $C$.

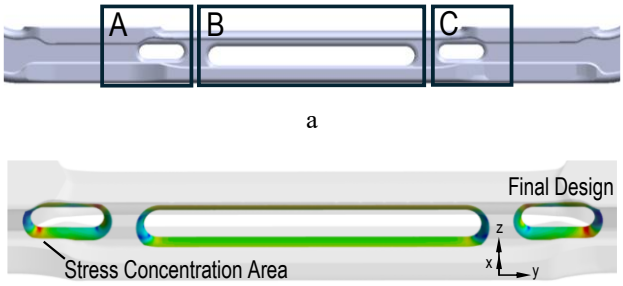


a




b

Fig. 19 Stress distributions on the slots: a – examined regions, b – stress concentration regions

In the notch factor calculation for critical zones, the maximum equivalent stress values corresponding to the same nodal point in the initial and final design models were determined for four points selected from high stress concentration regions. Using these stress values, $K_t$ coefficients were calculated according to FEA. The stress values given in Fig. 20 are given in proportion to the values obtained from the final design by taking the equivalent stress at that point of the initial model as reference. The radii of the geometric structures in region $A$ were considered as notch radius. The notch sensitivity ($q$) given in the literature for steel structures was found to be 0.9 using this radius [29]. $K_f$ value was determined according to Eq. (10) using the $K_t$ and $q$ values calculated. Then, using this $K_f$ value, the fatigue – strength – reduction factor ($k_e$) was calculated according to Eq. (11). The fatigue limit ($S_e$) values were determined for $A$ and the lower regions of the axle body using Eq. (6).

$$k_e = \frac{1}{K_f}. \tag{11}$$

Most fatigue tests involve alternating tensile and compressive stresses, usually applied by cyclic bending [32]. There are various terms used to describe these stresses such as mean stress ($\sigma_m$), stress amplitude ($\sigma_a$). These terms which can be expressed as Eq. (12) and Eq. (13), play an important role in material life prediction and fatigue analyses:

$$\sigma_m = \frac{\sigma_{max} + \sigma_{min}}{2}, \tag{12}$$

$$\sigma_a = \frac{\sigma_{max} - \sigma_{min}}{2}. \quad (13)$$

Here, $\sigma_{max}$ and $\sigma_{min}$ are the highest and lowest stress values in the cycle, respectively. In this study, $\sigma_{min}$ is assumed to be zero. The main reason for this is that it is not possible for a negative vertical contact force value to occur at the wheels during a severe bump motion. In other words, when the tire – road surface contact is lost, $\sigma_{min}$ is equal to zero. In the literature, it has been observed that axle fatigue diagrams vary between a small stress value close to zero and a maximum value and therefore this approach is suitable for application [33, 34]. Goodman – Haigh diagrams were constructed for eight points selected from the critical zones of the initial and final design. In the Goodman – Haigh diagrams shown in Fig. 20, c, a yield line was defined by connecting the yield strength ($\sigma_y$) points. The $S_e$ values calculated for the eight selected points were combined with the tensile strength in the tensile zone and projected on the compression side. As a result, the infinite life region shown in the figure was obtained for the axle beam.

When the graphs are analysed, it is seen that the stresses obtained at the critical regions of the final design remain in the infinite life (safe) region. As a result, 14.2% mass reduction was realised in the axle beam. In addition to the critical load case (Vertical Bump ($3G$)), the side force acting on the tyre contact patch during cornering manoeuvre and the moment generated by it cause stress concentration in the neck region of the axle beam. In the literature, it is known that stress concentration in these regions leads to fracture failure in some cases [35].

Therefore, the final design is compared with the reference model in Fig. 21 by considering these two critical load cases. Here, the stresses in all critical regions were found as a ratio to the yield stress. According to the results of the analyses, it is seen that the stresses are significantly below the yield stress. Thus, the final design is considered to be safe.

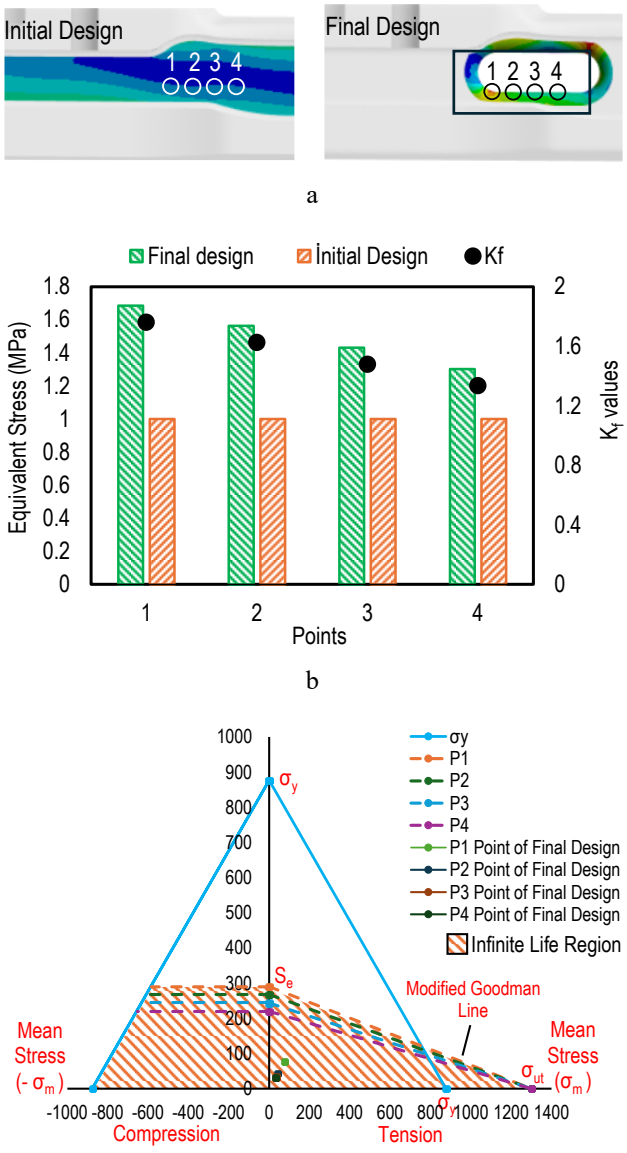


Fig. 20 Fatigue life evaluation: a – selected point on axle beam, b – $K_f$ values obtained for the stress concentration region, c – Goodman – Haigh diagram of the critical stress region

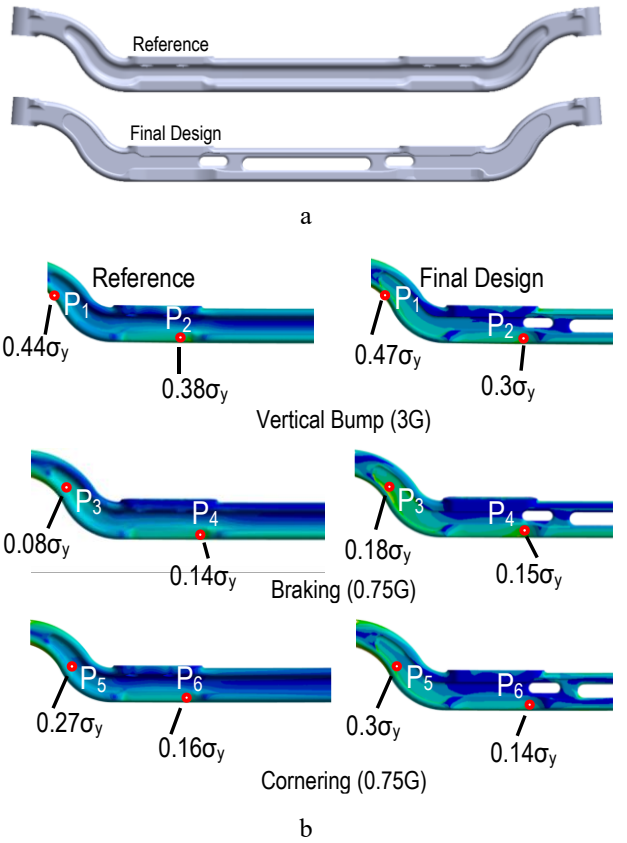


Fig. 21 Stress distribution on the final design: a – comparison of the reference and final designs, b – stress values according to critical loading conditions

While the mass of the reference axle beam in use was 104.2 kg, the final geometry obtained as a result of optimisation was determined as 89.4 kg. Accordingly, a total mass reduction of 14.8 kg was achieved. Due to this mass gain, for every 6 axle beams produced, one extra axle beam with final geometry can be produced. According to the data received from the axle manufacturer company, the axle beam examined in this study has an annual production capacity of approximately 48,000 units. Thanks to the mass gain achieved as a result of the optimisation study, it was seen that there is a potential to produce approximately 8,000 additional axle housings using the same amount of material.

## 5. Conclusions

This paper outlines the topology optimization and Design of Experiments (DoE) based mass reduction of a rigid front axle of a heavy commercial vehicle. Firstly, various Finite Element (FE) analyses were performed to determine the stress concentrations of the axle beam in current use at various loading conditions found in the literature. Then, topology optimization was applied to determine the regions where mass reduction is possible at the selected critical loading condition. Design parameters were determined based on the results of the analyses. A parametric study was also performed on the axle beam using the DoE – RSM approach. The results obtained from this study are summarized below:

By using the stresses in the FEA results of the geometries created on the axle body, the Goodman – Haigh diagram was created and mass reduction was carried out to meet the infinite life criterion. With the design change made in the lower flange of the axle beam, the stress value was reduced by approximately 70%. As a result of this study, the mitigation work carried out with the selected parameters reduced the mass by 14.2% without creating a new damage mode or zone.

In order to numerically examine the gain to be achieved during the production of the new design, production values obtained from the manufacturer were used. According to the data obtained from the axle manufacturer company, this axle type has been produced 4,000 units per month on average since 2007. This corresponds to an annual production capacity of approximately 48,000 units. As a result of the optimisation study, it was determined that approximately 8,000 additional axle beams could be produced with the same amount of material thanks to the mass gain.

This study shows that by using FE analyses and optimisation techniques, results can be obtained that can provide significant improvements to manufacturers in the design of components with high market value. It also demonstrates through a case study that failure analysis can be used effectively as a mass reduction and cost improvement tool.

## References


1. **Wimmer, H.** 1998. Modern Front Axle Systems for Low Floor Buses and Coaches, SAE Technical Paper: 982776. https://doi.org/10.4271/982776.
2. **Wimmer, H.; Alsdorf, F.** 2006. Modern front axle systems for city buses. ATZ Worldwide, 108(3): 2-5. https://doi.org/10.1007/BF03224810.
3. **Datti, D. H.; Nallamothu, R. B.; Mitiku, G.; Siraj, A.; Fentaw, G.** 2021. Design and Analysis of Front Axle of Truck at Different Driving Conditions. In: Jha, K.; Gulati, P.; Tripathi, U.K. (eds) Recent Advances in Sustainable Technologies: Select Proceedings of ICAST 2020: 195-206. https://doi.org/10.1007/978-981-16-0976-3_18.
4. **Hilgers, M.** 2023. Chassis and Axles, 2nd ed. Springer-Verlag GmbH. 80p. https://doi.org/10.1007/978-3-662-66614-2.
5. **Reimpell, J.; Stoll, H.; Betzler, J.** 2001. The Automotive Chassis: Engineering Principles, 2nd ed. Oxford: Elsevier. 444p.
6. **Ruban, M.; Sivaganesan, S.** 2016. Design analysis and optimization of front axle for commercial vehicle using CAE, ARPN Journal of Engineering and Applied Sciences 11(13): 8511-8516.
7. **Wang, X.; Hua, L.** 2021. Finite element study on microstructure evolution and grain refinement in the forging process of automotive front axle beam, The International Journal of Advanced Manufacturing Technology 114: 1179-1187. https://doi.org/10.1007/s00170-021-06914-w.
8. **Heißing, B.; Ersoy, M.** 2011. Chassis Handbook: Fundamentals, Driving Dynamics, Components, Mechatronics, Perspectives. – Berlin: Springer Science & Business Media. 591p. https://doi.org/10.1007/978-3-8348-9789-3.
9. **Topac, M. M.; Atak, M.** 2016, October. Optimal design of a rigid front axle beam for trucks, In: 1st International Mediterranean Science and Engineering Congress (IMSEC 2016): 1341-1349.
10. **Topaç, M. M.; Bahar, İ.; Kuralay, N. S.** 2016. Mass and stress optimisation of a multi-purpose vehicle front axle differential housing for various driving conditions, Duzce University Journal of Science and Technology 4(2): 501–513.
11. **Mathur, A.; Kurna, S.** 2015. Weight optimization of axle beam using OptiStruct, Altair Technology Conference, India.
12. **Güler, A.; Kuralay, N.S.; Topaç, M.M.** 2012. Ağır ticari araçlarda kullanılan arka aks döküm kovanının sac diferansiyel kovanına dönüştürülmesi (Transformation of a casting rear axle housing to fabricated axle housing), 6 Otomotiv Teknolojileri Kongresi (OTEKON 2012), Bursa, Turkey (in Turkish).
13. **Loosle, D. G.; Leon, P. F.; Danielson, C. R.** 1980. One Piece Stamped I-Beam Axle (No. 801425). SAE Technical Paper. https://doi.org/10.4271/801425.
14. **Neugebauer, J. R.; Grubisic, V.; Fischer, G.** 1989. Procedure for design optimization and durability life approval of truck axles and axle assemblies (No. 892535). SAE Technical Paper. https://doi.org/10.4271/892535.
15. **Jazar, R. N.** 2008. Vehicle Dynamics: Theory and Application. New York: Springer. 1015p. https://doi.org/10.1007/978-0-387-74244-1.
16. **Mitschke, M.** 1972. Dynamik der Kraftfahrzeuge. Berlin: Springer. 529p. (in German). https://doi.org/10.1007/978-3-662-11585-5.
17. **Bendsoe, M. P.; Sigmund, O.** 2004. Topology Optimization: Theory, Methods, and Applications 2nd ed. Berlin: Springer. 370p. https://doi.org/10.1007/978-3-662-05086-6.
18. **Johnsen, S.** 2013. Structural topology optimization: basic theory, methods and applications (Master's thesis, Institutt for Produktutvikling og Materialer). 197p.
19. **Sigmund, O.; Maute, K.** 2013. Topology optimization approaches: a comparative review, Structural and Multidisciplinary Optimization 48(6): 1031-1055. https://doi.org/10.1007/s00158-013-0978-6.
20. **Petersson, J.** 1999. A Finite Element Analysis of Optimal Variable Thickness Sheets, SIAM Journal on Numerical Analysis 36(6): 1759-1778. https://doi.org/10.1137/S0036142996313968.

21. **Amago, T.** 2002. Sizing optimization using response surface method in FOA. R&D Review of Toyota CRDL 37(1): 1-7.
22. **Guo, X.; Yan, Z.; Yu, J.** 2024. Failure analysis of kingpin hole on front axle of mining truck based on finite element analysis, Engineering Failure Analysis 166: 108888. https://doi.org/10.1016/j.engfailanal.2024.108888.
23. **Eryürek, B.** 1993. Hasar Analizi. İstanbul: Birsen Yayınevi. (In Turkish).
24. **Tanrıkulu, B.; Karakuzu, R.** 2020. Fatigue life prediction model of WC-Co cold forging dies based on experimental and numerical studies, Engineering Failure Analysis 118: 104910. https://doi.org/10.1016/j.engfailanal.2020.104910.
25. **Arcieri, E. V.; Baragetti, S.; Božić, Ž.** 2024. Failure analysis of Ti6Al4V titanium alloy under fatigue loading: An experimental and numerical study, Engineering Failure Analysis 164: 108715. https://doi.org/10.1016/j.engfailanal.2024.108715.
26. **Zhu, G.; Li, Y. J.; Zhu, M. L.; Xuan, F. Z.** 2024. Safety assessment of interaction behavior of high cycle and very high cycle fatigue with creep at high temperature, International Journal of Pressure Vessels and Piping 210: 105235. https://doi.org/10.1016/j.ijpvp.2024.105235.
27. **Sendeckyj, G. P.** 2001. Constant life diagrams – a historical review, International Journal of Fatigue 23(4): 347-353. https://doi.org/10.1016/S0142-1123(00)00077-3.
28. **Haigh, B. P.** 1929. The relative safety of mild and high-tensile alloy steels under alternating and pulsating stresses, Proceedings of the Institution of Automobile Engineers 24(1): 320-362.
29. **Shigley, J. E.; Mitchell, L. D.; Saunders, H.** 1985. Mechanical Engineering Design. – New York: McGraw-Hill.
30. **Yüksel, M.** 2003. Malzeme Bilgisi 1. 1. cilt. – Ankara: TMMOB Makina Mühendisleri Odası (in Turkish).
31. **Subaşı, M.; Karataş, Ç.** 2011. The investigation of residual stresses effect on the hardness of tempered AISI 4140 steel, Politeknik Dergisi 14(4): 289-295.
32. **Hosford, W. F.** 2009. Fatigue. In: Mechanical Behavior of Materials: 275-301. -Cambridge: Cambridge University Press. https://doi.org/10.1017/CBO9780511810923.018.
33. **Topaç, M. M.; Günal, H.; Kuralay, N. S.** 2009. Fatigue failure prediction of a rear axle housing prototype by using finite element analysis, Engineering Failure Analysis 16(5): 1474-1482. https://doi.org/10.1016/j.engfailanal.2008.09.016.
34. **Topaç, M. M.; Polat, K.; Seren, O.; Buldu, M. M.; Güzey, G.** 2024, November. Effect of stiffening rib location on failure tendency of a heavy-duty rear axle housing. In: International Congress of Automotive and Transport Engineering, pp. 212-221. – Cham: Springer Nature Switzerland. https://doi.org/10.1007/978-3-031-77627-4_18.
35. **Perumal, V.; Palanivelu, S.; Mookherjee, S. P.; Jindal, A. K.** 2012. Influence of Forging Process on Fatigue Properties of AISI 4140 Steel Axle Component, ASME Journal of Engineering Materials and Technology 134(1): 010909. https://doi.org/10.1115/1.4005405.

K. Polat, M. M. Topaç, U. Çoban

FAIL-SAFE MASS REDUCTION OF A HEAVY-DUTY FRONT AXLE USING TOPOLOGY OPTIMIZATION

S u m m a r y

A Topology Optimization and Design of Experiments (DoE) based mass reduction process for the rigid front axle of an in-use heavy commercial vehicle is summarized. Finite Element (FE) analyses were performed to determine the stress concentration regions of the axle beam for different loading conditions. Then, topology optimization was used to determine the regions where mass reduction is possible under critical loading condition. According to the results of the analyses, design parameters for the form and location of the holes were determined. A parametric study was carried out on the axle beam using the DoE – Response Surface Methodology (RSM) approach. The failure potential of these holes was evaluated with the help of Goodman – Haigh diagram. The results showed that the total mass can be reduced by 14.2% without creating a new failure mode. Considering the annual production capacity of the axle studied, it is seen that approximately 8,000 additional axle beams can be produced using the same amount of material.

**Keywords:** fail-safe lightweight design, vehicle suspensions, rigid axle beam, topology optimisation, mass reduction, design of experiments.

Received September 30, 2025
Accepted December 15, 2025